Topological Phononic Crystals with One-Way Elastic Edge Waves

Pai Wang,[1] Ling Lu,[2] and Katia Bertoldi[1,3,*]
[1]Harvard John A. Paulson School of Engineering and Applied Sciences, Harvard University, Cambridge, Massachusetts 02138, USA
[2]Department of Physics, MIT, Cambridge, Massachusetts 02139, USA
[3]Kavli Institute, Harvard University, Cambridge, Massachusetts 02138, USA
(Received 3 April 2015; published 4 September 2015)

We report a new type of phononic crystals with topologically nontrivial band gaps for both longitudinal and transverse polarizations, resulting in protected one-way elastic edge waves. In our design, gyroscopic inertial effects are used to break the time-reversal symmetry and realize the phononic analogue of the electronic quantum (anomalous) Hall effect. We investigate the response of both hexagonal and square gyroscopic lattices and observe bulk Chern numbers of 1 and 2, indicating that these structures support single and multimode edge elastic waves immune to backscattering. These robust one-way phononic waveguides could potentially lead to the design of a novel class of surface wave devices that are widely used in electronics, telecommunication, and acoustic imaging.

DOI: 10.1103/PhysRevLett.115.104302 PACS numbers: 46.40.Cd, 46.40.Ff, 73.43.-f

Topological states in electronic materials, including the quantum Hall effect [1] and topological insulators [2,3], have inspired a number of recent developments in photonics [4,5], phononics [6–9], and mechanical metamaterials [10–13]. In particular, in analogy to the quantum anomalous Hall effect [14], one-way electromagnetic waveguides in two-dimensional systems have been realized by breaking time-reversal symmetry [15–18].

Very recently, unidirectional edge channels have been proposed for elastic waves using Coriolis force in a noninertial reference frame [19], but such a rotating frame is very difficult to implement in solid state devices. Moreover, one-way propagation of scalar acoustic waves has also been proposed by introducing rotating fluids [20–22]. However, it is important to recognize that elastic waves in solids have both transverse and longitudinal polarizations, while acoustic waves in fluids are purely longitudinal. As a result, it is challenging to achieve topological protection for elastic waves on an integrated platform.

Here, we present a robust strategy to create topologically nontrivial edge modes for both longitudinal and transverse polarizations in a solid medium. In particular, we introduce gyroscopic phononic crystals, where each lattice site is coupled with a spinning gyroscope that breaks time-reversal symmetry in a well-controlled manner. In both hexagonal and square lattices, gyroscopic coupling opens band gaps that are characterized by Chern numbers of 1 and 2. As a result, at the edge of these lattices both single-mode and multimode one-way elastic waves are observed to propagate around arbitrary defects without backscattering.

To start, we consider a hexagonal phononic crystal with equal masses ($m_2 = m_1$) connected by linear springs [red and black rods in Figs. 1(a) and 1(b)]. The resulting unit cell has 4 degrees of freedom specified by the displacements of m_1 and m_2 ($\mathbf{U} = [u_x^{m_1}, u_y^{m_1}, u_x^{m_2}, u_y^{m_2}]$). Consequently, there are a total of four bands in the band structure [Fig. 1(c)]. Note that this is the minimal number of bands required to open a complete band gap, since the first two elastic dispersion bands are pinned at zero frequency. The phononic band structures are calculated by solving the dispersion equation [23]

$$[\mathbf{K}(\boldsymbol{\mu}) - \omega^2\mathbf{M}]\mathbf{U} = \mathbf{0} \tag{1}$$

for wave vectors $\boldsymbol{\mu}$ within the first Brillouin zone. Here, ω denotes the angular frequency of the propagating wave and $\mathbf{M} = \mathrm{diag}\{m_1, m_1, m_2, m_2\}$ is the mass matrix. Moreover, $\mathbf{K}$ is the 4×4 stiffness matrix and is a function of the Bloch wave vector $\boldsymbol{\mu}$. The band structure of this simple lattice is shown in Fig. 1(c). As expected, in the long wavelength regime (near the G point) the first and second bands correspond to transverse and longitudinal modes, respectively, while for short wavelengths (near K points) all modes are found to have mixed polarization (detailed analysis of the modal polarization is given in Supplemental Material [24]). Moreover, we observe a quadratic degeneracy between the third and fourth bands at the center of the Brillouin zone and a complete gap between the second and third bands due to the lack of inversion symmetry. However, this gap is topologically trivial, since time-reversal symmetry is not broken and the Chern numbers of the bands are all zero.

In order to break time-reversal symmetry, we introduce gyroscopic coupling [25,26,30] and attach each mass in the lattice to the tip of the rotational axis of a gyroscope, as shown in Fig. 1(d). Note that the other tip of the gyroscope is pinned to the ground to prevent any translational motion, while allowing for free rotations. Because of the small-amplitude in-plane waves propagating in the phononic

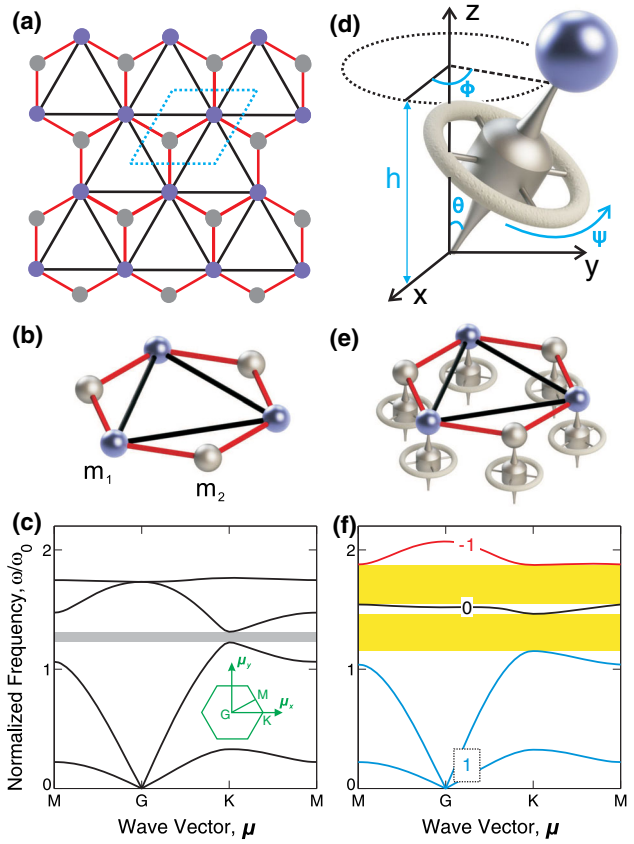

FIG. 1 (color online). Ordinary and gyroscopic phononic crystals: (a) Schematic of the hexagonal lattice. The blue and grey spheres represent concentrated masses m_1 and $m_2 = m_1$, respectively. The red and black straight rods represent massless linear springs with stiffness k_1 and $k_2 = k_1/20$, respectively. The dashed cell is the primitive cell of the lattice. (b) Unit cell for the ordinary (nongyroscopic) phononic crystal. (c) Band structure of the ordinary (nongyroscopic) phononic crystal. The inset is the Brillouin zone. (d) Schematic of a gyroscope with the top tip pinned to a mass in the lattice. (e) Unit cell for the gyroscopic phononic crystal. (f) Band structure of the gyroscopic phononic crystal ($\alpha_1 = \alpha_2 = 0.3m_1$) with the Chern numbers labeled on the bulk bands. The frequencies are normalized by $\omega_0 = \sqrt{k_1/m_1}$.

lattice, the magnitude of the tip displacement of the each gyroscope is given by

$$U_{\mathrm{tip}} = h\sin\theta \approx h\theta = h\Theta e^{i\omega t} \quad \text{for } |\Theta| \ll 1, \tag{2}$$

where h and θ denote the height and nutation angle of the gyroscope [Fig. 1(d)] and Θ is the amplitude of the harmonic change in θ. Interestingly, the coupling between the mass in the lattice and the gyroscope induces an in-plane gyroscopic inertial force perpendicular to the direction of U_{tip} [24,25,27]:

$$F_g = \pm i\omega^2 \alpha U_{\mathrm{tip}}, \tag{3}$$

where α is the spinner constant that characterizes the strength of the rotational coupling between two independent inertias in the 2D plane. As a result, the mass matrix in Eq. (1) becomes

$$\tilde{\mathbf{M}} = \mathbf{M} + \begin{pmatrix} 0 & i\alpha_1 & 0 & 0 \\ -i\alpha_1 & 0 & 0 & 0 \\ 0 & 0 & 0 & i\alpha_2 \\ 0 & 0 & -i\alpha_2 & 0 \end{pmatrix}, \tag{4}$$

where α_1 and α_2 denote the spinner constants of the gyroscopes attached to m_1 and m_2, respectively. We note that the imaginary nature of the gyroscopic inertial effect indicates directional phase shifts with respect to the tip displacements, which breaks time-reversal symmetry.

We now consider the band structure of the gyroscopic hexagonal lattice. Interestingly, we find that the original band gap between the second and third bands first closes into a Dirac cone at the K points and then reopens as we gradually increase the magnitude of α_1 and α_2. In particular, for $\alpha_1 = \alpha_2 = 0.07m_1$ the gap is closed and a pair of Dirac cones at K points emerges, while for $\alpha_1 = \alpha_2 = 0.3m_1$ the gap reopens, as shown in Fig. 1(f). We also note that this topological transition at $\alpha_1 = \alpha_2 = 0.07m_1$ is accompanied by a band inversion [9] between the second and third bands near the K points (the complete process of this topological transition is shown in the Supplemental Material [24]). Since each Dirac point carries a Berry phase of π and there is a pair of Dirac cones in the first Brillouin zone [31], we expect the total exchange of Berry curvature between the two bands to be 2π, resulting in one chiral edge state in the gap between the second and third bands. Similarly, we also observe that the quadratic degeneracy found for the ordinary lattice between the third and fourth bands at the Brillouin zone center [see Fig. 1(c)] is opened into a full band gap when gyroscopic coupling is introduced [see Fig. 1(f)]. Since such a quadratic touching carries a 2π Berry phase [32], there should be one chiral edge state in the gap between the third and fourth bands. Importantly, the fact that band gaps in Fig. 1(f) are topologically nontrivial is confirmed by the nonzero Chern numbers labeled on the bands (the calculations conducted to compute these topological invariants are detailed in the Supplemental Material [24]). Therefore, in the frequency ranges of these nontrivial band gaps, we expect gapless one-way edge states, whose number is dictated by the sum of Chern numbers below the band gap, in agreement with our intuitive arguments of Berry phase.

To verify the existence of such one-way edge states, we perform one-dimensional (1D) Bloch wave analysis on a supercell comprising 20×1 unit cells, assuming free boundary conditions for the top and bottom edges. In full agreement with the bulk Chern numbers, the band structure of the supercell shows one one-way edge mode on each edge in both band gaps. For modes bound to the top edge [Fig. 2(b)], the propagation can only assume negative group

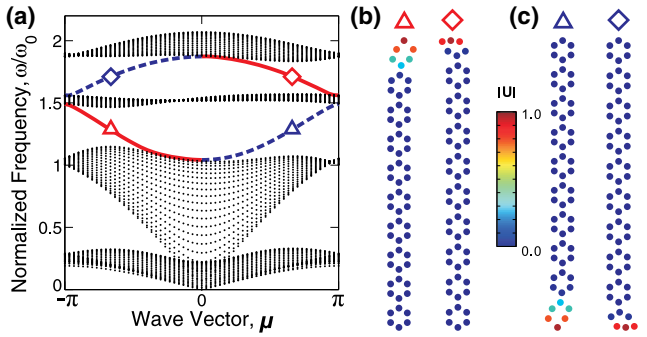

FIG. 2 (color online). Edge modes in gyroscopic phononic crystal: (a) 1D band structure showing bulk bands (black dots) and edge bands (colored lines). Red solid lines represent edge modes bound to the top boundary, while blue dashed lines represent edge modes bound to the bottom boundary. (b) Modal displacement fields of top edge states with negative group velocities. (c) Modal displacement fields of bottom edge states with positive group velocities.

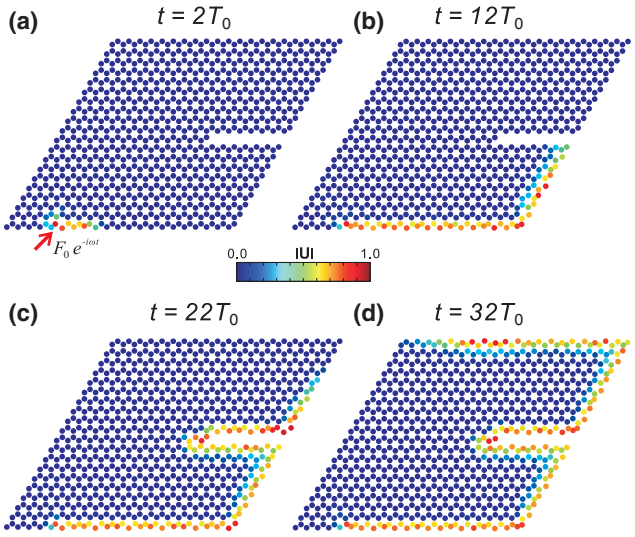

FIG. 3 (color online). Transient response of a gyroscopic phononic crystal consisting of 20×20 unit cells with a line defect on the right boundary: Snapshots of the displacement field at (a) $t = 2T_0$, (b) $t = 12T_0$, (c) $t = 22T_0$ and (d) $t = 32T_0$, where $T_0 = \sqrt{m_1/k_1}$ is the characteristic time scale of the system. Starting from $t = 0$, a time-harmonic excitation force $\mathbf{F}(t) = [F_x(t), F_y(t)] = [1, 1]F_0 e^{-i\omega t}$ is prescribed at the site indicated by the red arrow.

velocities [red solid lines with negative slope in Fig. 2(a)]. On the other hand, the modes bound to the bottom edge [Fig. 2(c)] possess positive group velocities [blue dashed lines with positive slope in Fig. 2(a)]. Since these edge modes are in the gap frequency range where no bulk modes may exist, they cannot scatter into the bulk of the phononic crystal. Furthermore, their unidirectional group velocities guarantee the absence of any backscattering and result in the topologically protected one-way propagation of vibration energy.

To show the robustness of these edge states, we conduct transient analysis on a finite sample comprising 20×20 unit cells with a line defect on the right boundary created by removing twelve masses and the springs connected to them [Fig. 3(a)]. A harmonic force excitation, $F_0 e^{-i\omega t}$, is prescribed at a mass site on the bottom boundary [red arrow in Fig. 3(a)] with frequency within the bulk band gap between the second and third bands ($\omega/\omega_0 = 1.3$). In Fig. 3 we plot snapshots of the velocity field at different time instances, $t/T_0 = 2$, 12, 22, and 32, where $T_0 = \sqrt{m_1/k_1}$ is the characteristic time scale of the system. Remarkably, because of their topological protection, the edge modes circumvent both the sharp corner and the line defect without any reflection. We note that, although the results presented in Fig. 3 are for a harmonic excitation with 45° inclination (i.e., $\mathbf{F}(t) = [F_x(t), F_y(t)] = [1, 1]F_0 e^{-i\omega t}$), the one-way edge propagations are not affected by the direction of the applied force (additional results are included in the Supplemental Material [24]).

Next, we investigate the effect of the lattice geometry and start with an ordinary square phononic crystal with masses m_1 connected by springs with elastic constant k_1. To make the lattice statically stable, we add an additional mass $m_2 = m_1$ at the center of each unit cell and connect it to its four adjacent m_1 masses by springs with elastic constant $k_2 = 2k_1$ [see Fig. 4(a)]. The band structure for this lattice [shown in Fig. 4(b)] contains a pair of threefold linear degeneracies among the first, second, and third bands at the X points of the Brillouin zone. Note that this type of degeneracy, consisting of a locally flat band and a Dirac point, is known as the "accidental Dirac point" or "Dirac-like cones" [33,34]. Interestingly, was previously found to occur at the Brillouin zone center and very sensitive to the system parameters, in our lattice it robustly appears at the X points when $m_1 = m_2$. Upon the introduction of gyroscopic inertial effects ($\alpha_1 = \alpha_2 = 0.3m_1$), these threefold degenerate points are lifted and a gap is created between the second and third bands [Fig. 4(c)]. The Chern number of the two bulk bands below the gap is two, predicting the existence of two topological edge states. The presence of multimode one-way elastic waves is consistent with the fact that the Berry phase associated with such a three-band degeneracy is 2π [35], resulting in a total exchange of the Berry curvature of 4π when gapping two of these points in the Brillouin zone [36]. In Figs. 4(d) and 4(e), we plot the band structure of the corresponding 20×1 supercell, highlighting two one-way edge modes and their modal displacement fields.

To summarize, we demonstrated that gyroscopic phononic crystals can support topologically nontrivial gaps, within which the edge states are unidirectional and immune to backscattering. The transient analysis confirmed that the propagations of such topological edge waves are robust

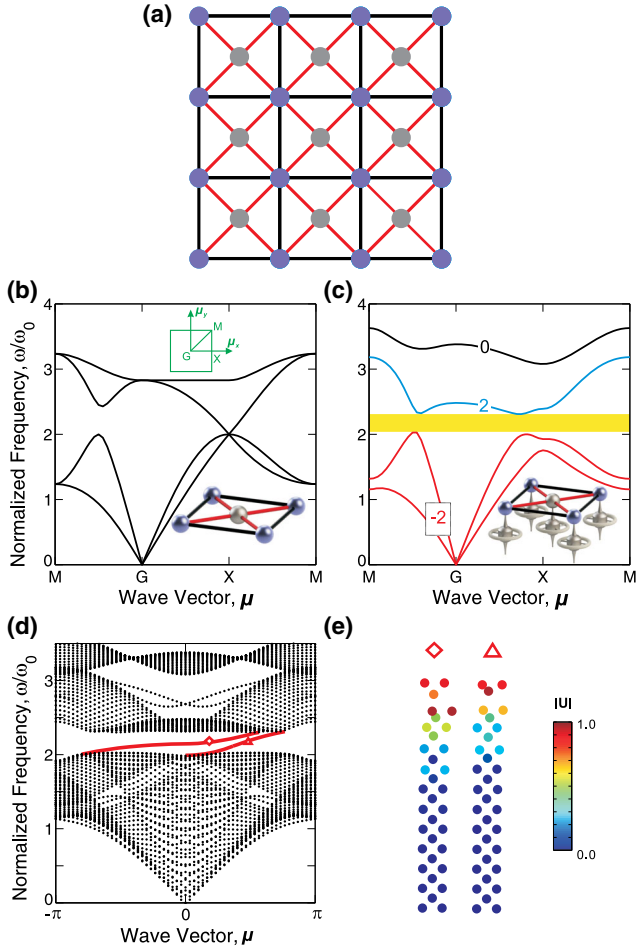

FIG. 4 (color online). Square lattice results: (a) Schematic of the square lattice. The blue and grey spheres represent concentrated masses m_1 and $m_2 = m_1$, respectively. The black and red straight rods represent massless linear springs with stiffness k_1 and $k_2 = 2k_1$, respectively. (b) Band structure of the ordinary (nongyroscopic) phononic crystal. The insets are the Brillouin zone and the unit cell. (c) Band structure of the gyroscopic phononic crystal ($\alpha_1 = \alpha_2 = 0.3m_1$) with the Chern numbers labeled on the bulk bands. Frequencies are normalized by $\omega_0 = \sqrt{k_1/m_1}$. The inset is the unit cell. (d) 1D band structure showing bulk bands (black dots) and two topological edge bands (red solid lines) bound to the top boundary. Note that the edge bands that are bound to the bottom boundary are not shown here. (e) Modal displacement fields of the edge states shown in (d).

against large defect and sharp corners. Moreover, we showed, for the first time, the multimode one-way states (Chern number $= \pm 2$) in phononic systems, opening more avenues for the design of future topological waveguides and devices. While in this study we developed a comprehensive framework for the design and analysis of topological phononic crystals, we recently became aware of a parallel effort in which time-reversal symmetry breaking in a gyroscopic system has been theoretically analyzed and experimentally demonstrated [37].

Finally, we note that phononic crystals [38,39] and acoustic metamaterials [40–44] that enable manipulation and control of elastic waves have received significant interest in recent years [23,45], not only because of their rich physics, but also for their broad range of applications [46–58]. Interestingly, the edge wave modes in phononic crystals are important in many scenarios [59–62], including vibration control [63] and acoustic imaging [54]. However, most of the reported studies have focused on topologically trivial surface waves that can be easily scattered or localized by defects [59]. Therefore, the work reported here could open new avenues for the design of phononic devices with special properties and functionalities on edges, surfaces, and interfaces.

This work has been supported by NSF through Grants No. CMMI-1120724, No. CMMI-1149456 (CAREER) and the Materials Research Science and Engineering Center (DMR-1420570). K. B. acknowledges start-up funds from the Harvard School of Engineering and Applied Sciences and the support of the Kavli Institute and Wyss Institute at Harvard University. L. L. was supported in part by U.S.A.R.O. through the ISN under Contract No. W911NF-13-D-0001, in part by the MRSEC Program of the NSF under Award No. DMR-1419807 and in part by the MIT S3TEC EFRC of DOE under Grant No. DE-SC0001299. The authors are also grateful to Scott Skirlo, Timothy H. Hsieh, and Dr. Filippo Casadei for inspirational discussions and to Dr. Farhad Javid and Xin You for their support with graphics.

*Corresponding author.
bertoldi@seas.harvard.edu

[1] K. von Klitzing, Rev. Mod. Phys. **58**, 519 (1986).
[2] M. Z. Hasan and C. L. Kane, Rev. Mod. Phys. **82**, 3045 (2010).
[3] X.-L. Qi and S.-C. Zhang, Rev. Mod. Phys. **83**, 1057 (2011).
[4] F. D. M. Haldane and S. Raghu, Phys. Rev. Lett. **100**, 013904 (2008).
[5] L. Lu, J. D. Joannopoulos, and M. Soljačić, Nat. Photonics **8**, 821 (2014).
[6] E. Prodan and C. Prodan, Phys. Rev. Lett. **103**, 248101 (2009).
[7] L. Zhang, J. Ren, J.-S. Wang, and B. Li, Phys. Rev. Lett. **105**, 225901 (2010).
[8] R. Süsstrunk and S. D. Huber, Science **349**, 47 (2015).
[9] M. Xiao, G. Ma, Z. Yang, P. Sheng, Z. Zhang, and C. Chan, Nat. Phys. **11**, 240 (2015).
[10] K. Sun, A. Souslov, X. Mao, and T. Lubensky, Proc. Natl. Acad. Sci. U.S.A. **109**, 12369 (2012).
[11] C. Kane and T. Lubensky, Nat. Phys. **10**, 39 (2014).
[12] J. Paulose, B. G.-g. Chen, and V. Vitelli, Nat. Phys. **11**, 153 (2015).
[13] B. G.-g. Chen, N. Upadhyaya, and V. Vitelli, Proc. Natl. Acad. Sci. U.S.A. **111**, 13004 (2014).
[14] F. D. M. Haldane, Phys. Rev. Lett. **61**, 2015 (1988).

[15] Z. Wang, Y. D. Chong, J. D. Joannopoulos, and M. Soljačić, Phys. Rev. Lett. **100**, 013905 (2008).

[16] Z. Wang, Y. Chong, J. Joannopoulos, and M. Soljačić, Nature (London) **461**, 772 (2009).

[17] S. A. Skirlo, L. Lu, and M. Soljačić, Phys. Rev. Lett. **113**, 113904 (2014).

[18] S. A. Skirlo, L. Lu, Y. Igarashi, J. Joannopoulos, and M. Soljacic, arXiv:1504.04399.

[19] Y.-T. Wang, P.-G. Luan, and S. Zhang, New J. Phys. **17**, 073031 (2015).

[20] R. Fleury, D. L. Sounas, C. F. Sieck, M. R. Haberman, and A. Alù, Science **343**, 516 (2014).

[21] Z. Yang, F. Gao, X. Shi, X. Lin, Z. Gao, Y. Chong, and B. Zhang, Phys. Rev. Lett. **114**, 114301 (2015).

[22] X. Ni, C. He, X.-C. Sun, X.-p. Liu, M.-H. Lu, L. Feng, and Y.-F. Chen, New J. Phys. **17**, 053016 (2015).

[23] M. I. Hussein, M. J. Leamy, and M. Ruzzene, Appl. Mech. Rev. **66**, 040802 (2014).

[24] See Supplemental Material at http://link.aps.org/supplemental/10.1103/PhysRevLett.115.104302 for additional results and detailed derivations and calculation procedures, which includes Refs. [9,24–26,27,28].

[25] M. Brun, I. S. Jones, and A. B. Movchan, Proc. R. Soc. A **468**, 3027 (2012).

[26] G. Carta, M. Brun, A. Movchan, N. Movchan, and I. Jones, Int. J. Solids Struct. **51**, 2213 (2014).

[27] H. Goldstein, C. Poole, and J. Safko, *Classical Mechanics*, 3rd ed. (Addison Wesley, San Francisco, 2002).

[28] P. Wang and K. Bertoldi, in *Towards Phononic Topological Insulators, APS March Meeting*, A42.11 (2014), http://meetings.aps.org/link/BAPS.2014.MAR.A42.11.

[29] T. Fukui, Y. Hatsugai, and H. Suzuki, J. Phys. Soc. Jpn. **74**, 1674 (2005).

[30] G. W. Milton and J. R. Willis, Proc. R. Soc. A **463**, 855 (2007).

[31] Note that on the boundary of the first Brillouin zone of the hexagonal lattice there are six Dirac points. However, since at each point only one third of the Dirac cone is included in the first Brillouin zone, we have a pair of Dirac cones in total.

[32] Y. D. Chong, X.-G. Wen, and M. Soljačić, Phys. Rev. B **77**, 235125 (2008).

[33] F. Liu, X. Huang, and C. Chan, Appl. Phys. Lett. **100**, 071911 (2012).

[34] X. Huang, Y. Lai, Z. H. Hang, H. Zheng, and C. Chan, Nat. Mater. **10**, 582 (2011).

[35] J. Mei, Y. Wu, C. T. Chan, and Z.-Q. Zhang, Phys. Rev. B **86**, 035141 (2012).

[36] Note that on the boundary of the first Brillouin zone of the square lattice there are four equivalent X points. However, since at each point only one half of the three-band degeneracy is included in the first Brillouin zone, we have a pair of three-band degeneracies in total.

[37] L. M. Nash, D. Kleckner, A. Read, V. Vitelli, A. M. Turner, and W. T. Irvine, arXiv:1504.03362.

[38] M. Sigalas and E. Economou, Solid State Commun. **86**, 141 (1993).

[39] M. S. Kushwaha, P. Halevi, L. Dobrzynski, and B. Djafari-Rouhani, Phys. Rev. Lett. **71**, 2022 (1993).

[40] Z. Liu, X. Zhang, Y. Mao, Y. Zhu, Z. Yang, C. Chan, and P. Sheng, Science **289**, 1734 (2000).

[41] N. Fang, D. Xi, J. Xu, M. Ambati, W. Srituravanich, C. Sun, and X. Zhang, Nat. Mater. **5**, 452 (2006).

[42] Y. Ding, Z. Liu, C. Qiu, and J. Shi, Phys. Rev. Lett. **99**, 093904 (2007).

[43] Y. Lai, Y. Wu, P. Sheng, and Z. Zhang, Nat. Mater. **10**, 620 (2011).

[44] P. Wang, F. Casadei, S. Shan, J. C. Weaver, and K. Bertoldi, Phys. Rev. Lett. **113**, 014301 (2014).

[45] M. Maldovan and E. Thomas, *Periodic Materials and Interference Lithography for Photonics, Phononics and Mechanics* (Wiley-VCH, New York, 2009).

[46] M. Ruzzene, F. Scarpa, and F. Soranna, Smart Mater. Struct. **12**, 363 (2003).

[47] S. Phani, J. Woodhouse, and N. A. Fleck, J. Acoust. Soc. Am. **119**, 1995 (2006).

[48] J. O. Vasseur, A. Hennion, B. Rouhani, F. Duval, B. Dubus, and Y. Pennec, J. Appl. Phys. **101**, 114904 (2007).

[49] M. Kafesaki, M. M. Sigalas, and N. Garcia, Phys. Rev. Lett. **85**, 4044 (2000).

[50] Y. Pennec, B. Djafari-Rouhani, J. O. Vasseur, A. Khelif, and P. A. Deymier, Phys. Rev. E **69**, 046608 (2004).

[51] J. Mei, G. Ma, M. Yang, Z. Yang, W. Wen, and P. Sheng, Nat. Commun. **3**, 756 (2012).

[52] S. Brûlé, E. H. Javelaud, S. Enoch, and S. Guenneau, Phys. Rev. Lett. **112**, 133901 (2014).

[53] L.-S. Chen, C.-H. Kuo, and Z. Ye, Appl. Phys. Lett. **85**, 1072 (2004).

[54] J. Christensen, A. I. Fernandez-Dominguez, F. de Leon-Perez, L. Martin-Moreno, and F. J. Garcia-Vidal, Nat. Phys. **3**, 851 (2007).

[55] J. Li, L. Fok, X. Yin, G. Bartal, and X. Zhang, Nat. Mater. **8**, 931 (2009).

[56] D. Bigoni, S. Guenneau, A. B. Movchan, and M. Brun, Phys. Rev. B **87**, 174303 (2013).

[57] M. Maldovan, Phys. Rev. Lett. **110**, 025902 (2013).

[58] B. L. Davis and M. I. Hussein, Phys. Rev. Lett. **112**, 055505 (2014).

[59] M. Torres, F. R. Montero de Espinosa, D. Garcia-Pablos, and N. Garcia, Phys. Rev. Lett. **82**, 3054 (1999).

[60] D. Torrent and J. Sánchez-Dehesa, Phys. Rev. Lett. **108**, 174301 (2012).

[61] N. Boechler, J. K. Eliason, A. Kumar, A. A. Maznev, K. A. Nelson, and N. Fang, Phys. Rev. Lett. **111**, 036103 (2013).

[62] Y. Li, Y. Wu, and J. Mei, Appl. Phys. Lett. **105**, 014107 (2014).

[63] D. Torrent, D. Mayou, and J. Sánchez-Dehesa, Phys. Rev. B **87**, 115143 (2013).

Supplemental Materials to *Topological Phononic Crystals with One-Way Elastic Edge Waves*

Pai Wang,[1] Ling Lu,[2] and Katia Bertoldi[1,3]

[1]*Harvard John A. Paulson School of Engineering and Applied Sciences, Harvard University, Cambridge, Massachusetts 02138, USA*
[2]*Department of Physics, MIT, Cambridge, Massachusetts 02139, USA*
[3]*Kavli Institute, Harvard University, Cambridge, Massachusetts 02138, USA*

Contents

POLARIZATION CHARACTERISTICS

By calculating the dispersion relation for the lattices considered in this study, four Bloch modes (corresponding to four bands) for each $\mathbf{k}$ vector are obtained. Each Bloch mode takes the vector form $\mathbf{U} = [u_x^{m_1}, u_y^{m_1}, u_x^{m_2}, u_y^{m_2}]$, whose components are complex numbers:

$$U_1 = u_x^{m_1} = u_{x,re}^{m_1} + iu_{x,im}^{m_1}, \tag{S1}$$
$$U_2 = u_y^{m_1} = u_{y,re}^{m_1} + iu_{y,im}^{m_1}, \tag{S2}$$
$$U_3 = u_x^{m_2} = u_{x,re}^{m_2} + iu_{x,im}^{m_2}, \tag{S3}$$
$$U_4 = u_y^{m_2} = u_{y,re}^{m_2} + iu_{y,im}^{m_2}. \tag{S4}$$
$$\tag{S5}$$

The full expression of each vibrational mode in real space is then given by

$$\tilde{\mathbf{U}} = Re[\mathbf{U} \exp{(i\mathbf{k} \cdot \mathbf{r} - i\omega t)}], \tag{S6}$$

whose components can be rewritten as

$$\tilde{U}_j = Re[U_j] \cos(\Omega) - Im[U_j] \sin(\Omega) = A_j \cos(\Omega + B_j), \quad \text{for } j = 1, .., 4 \tag{S7}$$

where $\Omega = \mathbf{k} \cdot \mathbf{r} - \omega t$ and the j-th components of the amplitude vector $\mathbf{A}$ and phase vector $\mathbf{B}$ are defined as

$$A_j = \sqrt{Re[U_j]^2 + Im[U_j]^2}, \quad B_j = \arctan\left[\frac{Im[U_j]}{Re[U_j]}\right]. \tag{S8}$$

To better understand the polarization of the modes for the ordinary (non-gyroscopic) and gyroscopic hexagonal lattices, in Figs. S1 and S2 we plot the model displacement trajectories of m_1 and m_2 by varying Ω in Eqn. (S7) from 0 to 2π. Note that all the amplitudes have been normalized by $\max\limits_{j=1,2,3,4}(A_j)$.

In particular, in Fig. S1 we focus on the ordinary hexagonal lattice. As expected, in the long wavelength regime (near G-point) all four bands are linearly polarized. The first and forth bands correspond to transverse modes, while the second and third bands are longitudinal modes. Differently, for short wavelengths (near K-points) all modes are found to have mixed polarization. Note that in the Figure we report the modal polarization for four different wave vectors (G_K, K_1, K_2 and K) pointing in the same (horizontal) direction, but with different wavelengths (as indicated in the Brillouin zone on the top of the Figure). The results indicate a gradual transition from linearly polarized modes to modes with mixed polarization as the wavelength decreases.

In Fig. S2 we then report the modal displacement trajectories for the gyroscopic hexagonal lattice. By comparing the modal polarizations of the non-gyroscopic (Fig. S1) and gyroscopic (Fig. S2) hexagonal lattices, we can clearly see that a band inversion between the 2nd and 3rd bands occurs at K-points, indicating a topological transition. Furthermore, the modal mixing of the transverse and longitudinal polarizations for the 3rd and 4th bands near the G-point (at the G_K-point) also clearly indicates a topological transition occurring at the center of the Brillouin zone.

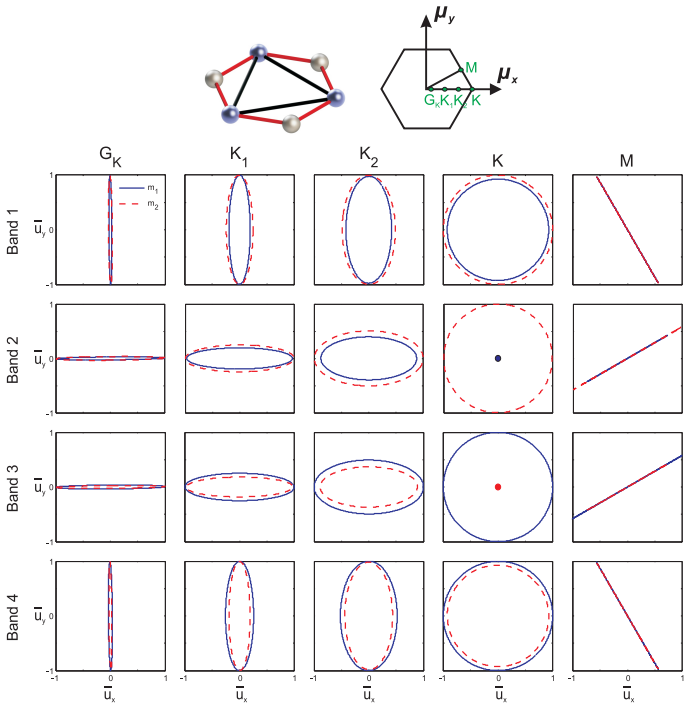

FIG. S1: **Modal polarization for the ordinary hexagonal lattice (i.e.** $\alpha_1 = \alpha_2 = 0$**):** Note that blue solid lines indicate polarization of m_1, while the red dashed lines represent the polarization of m_2. Results are reported for four **k**-space points on the G-K line and the M point, as indicated in the Brillouin zone on the top of the figure.

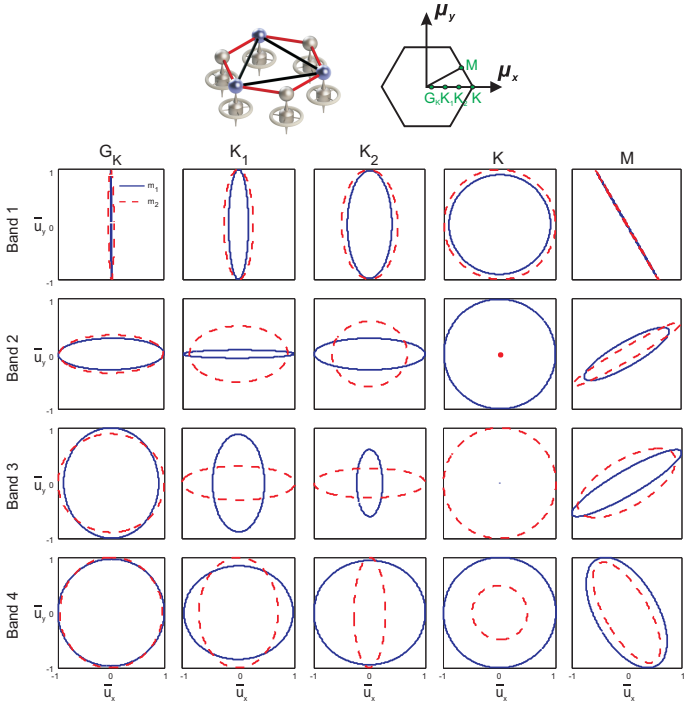

FIG. S2: **Modal polarization for the gyroscopic hexagonal lattice with** $\alpha_1 = \alpha_2 = 0.3m_1$**:** Note that blue solid lines indicate polarization of m_1, while the red dashed lines represent the polarization of m_2. Results are reported for four **k**-space points on the G-K line and the M point, as indicated in the Brillouin zone on the top of the figure.

BAND INVERSION IN GYROSCOPIC HEXAGONAL LATTICES

In Fig. S3 we report the evolution of the band structure for the gyroscopic hexagonal lattice considered in the main text. The band structures show that for $\alpha = \alpha_1 = \alpha_2 > 0$, a new topologically non-trivial gap between the 3rd and 4th bands is opened by lifting the quadratic degeneracy at G-point (the center of the Brillouin zone). Furthermore, we see that the size of this gap increases monotonically with α.

Differently, the gap observed in the ordinary (non-gyroscopic) lattice between the 2nd and 3rd bands initially gets narrower for increasing values of α. It eventually closes at $\alpha = 0.07m_1$, where a pair of Dirac-like linear crossing cones in the first Brillouin zone emerges. Note that there are six K-points due to six fold symmetry in the wave vector $\boldsymbol{\mu}$-space, but only one third of the cone at each K-point is included in the first Brillouin zone. Finally, for $\alpha > 0.07m_1$ a new (topologically nontrivial) gap is opened by lifting the pair of Dirac-like cones, so that the system is characterized by two topologically non-trivial gaps.

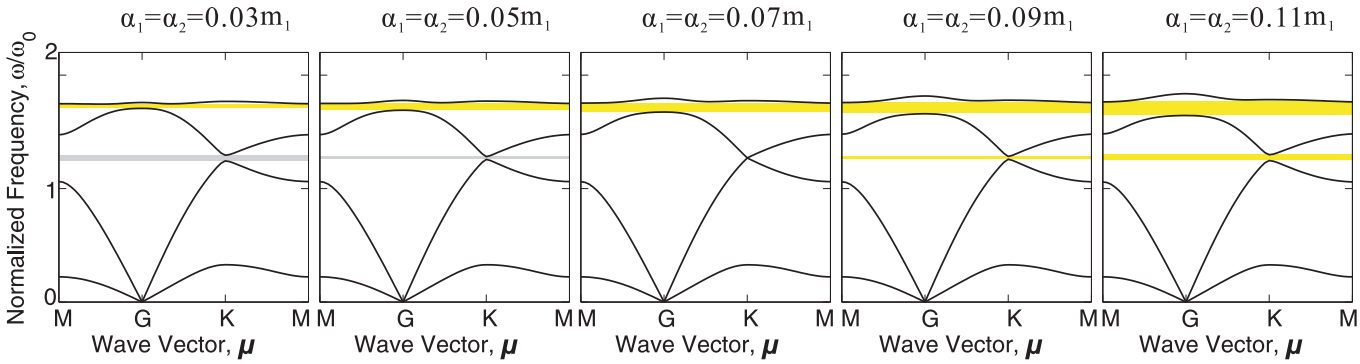

FIG. S3: **Evolution of the band structure for the gyroscopic hexagonal lattice as a function of α:** Note that the grey and yellow shaded areas highlight topologically trivial and non-trivial gaps, respectively.

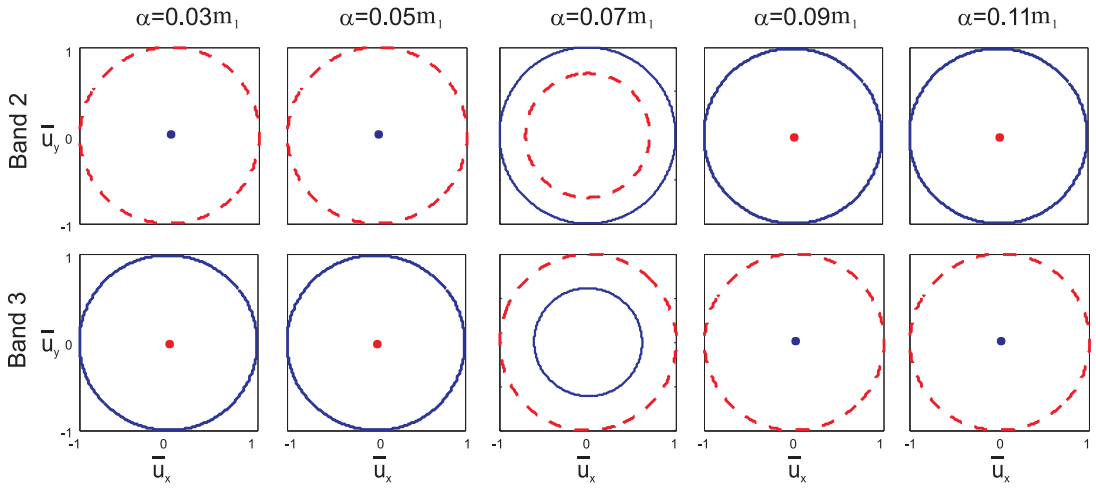

FIG. S4: **Evolution of the modal polarizations of 2nd and 3rd bands at K-points as a function of α**

Importantly, we also find that the topological transition is accompanied by a local band inversion near K-points. In fact, the results shown in Fig. S4 for the modal polarizations of m_1 and m_2 at K-points reveal that a local mode switching between the 2nd and 3rd bands occurs during the topological transition at $\alpha = 0.07m_1$. For $\alpha < 0.07m_1$ we find that the motion of m_2 dominates for the second band, while the motion of m_1 dominates for the third band. A switch occur at $\alpha = 0.07m_1$, so that when $\alpha > 0.07m_1$ we find that the motion of m_1 dominates for the second band, while the motion of m_2 dominates for the third band. We note that similar band inversion during topological phase change has recently been experimentally observed in one-dimensional acoustic systems [1].

TOPOLOGICAL PHASE DIAGRAM

To further clarify the process resulting in the formation of the topologically non-trivial gap between the 2nd and the 3rd bands, we also investigate the effect of symmetry breaking for spatial inversion (P) and time reversion (T). As shown in Fig. S5a, for a non-gyroscopic lattice with both P-T symmetries no gap is observed. Moreover, a Dirac-like crossing pair is found at the K point between the 2nd and the 3rd bands. When the time-reversal symmetry is broken by adding gyroscopes (Fig. S5b) the Dirac-like crossing pair is lifted and a topologically non-trivial gap forms (highlighted by the yellow shaded area in Fig. S5b).

On the other hand, when only the P-symmetry is broken by removing three black springs in the non-gyroscopic lattice (as shown in Fig. S5c), the Dirac-like crossing pair is also lifted, but the emerging gap (highlighted by the grey shaded area in Fig. S5c) is topologically trivial. Next, when also the T symmetry is broken by adding gyroscopes (Figs. S5d and e), we find that the band structure strongly depends on the relative strength of P-breaking and T-breaking. When P-breaking is dominant, only topologically trivial gaps are found. By contrast, when T-breaking is dominant, topologically non-trivial gaps form. Finally, we note that, when P-breaking and T-breaking are balanced (as in Fig. S5d), a Dirac-like crossing pair forms at the K point closing the band gap.

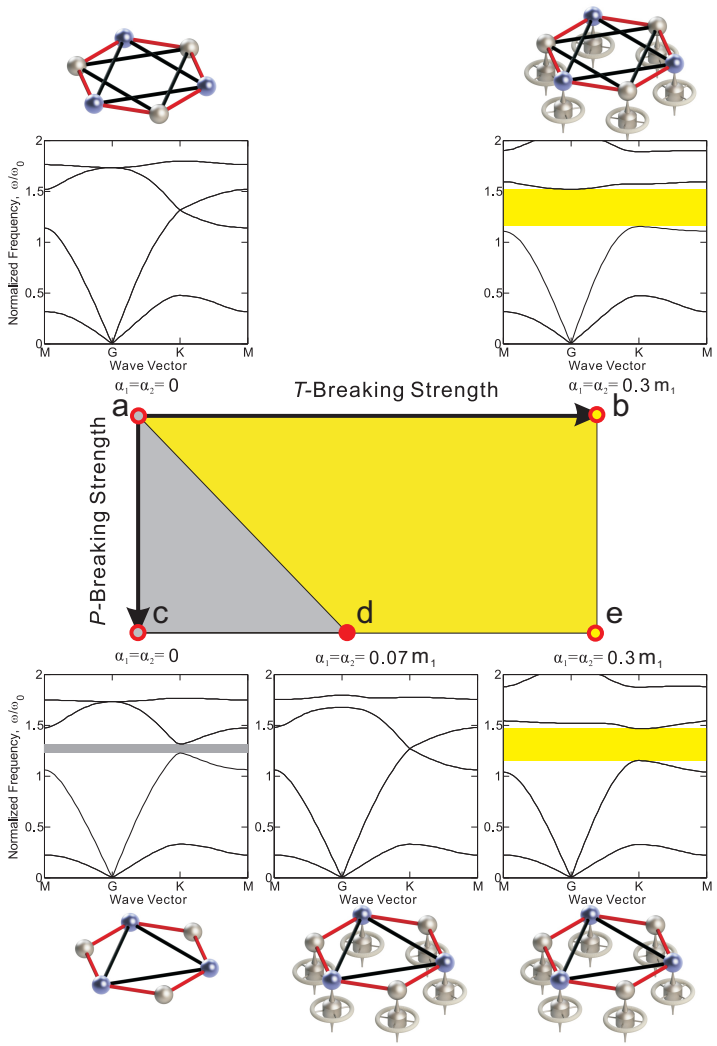

FIG. S5: **Topological phase diagram of the hexagonal phononic crystal.** **(a)** Phononic crystal with both P and T symmetries. The Dirac-like cones connecting the 2nd and 3rd bands at the K-point are protected by the PT symmetry. No gap is formed. **(b)** Topologically non-trivial gap emerges between the 2nd and 3rd bands due to broken T symmetry. **(c)** Topologically trivial gap emerges between the 2nd and 3rd bands due to broken P symmetry. **(d)** When P symmetry breaking and T symmetry breaking are balanced, the Dirac-like cones persist. **(e)** When the T symmetry breaking strength dominates the T symmetry breaking strength, the Dirac-like cones are lifted to form a topologically non-trivial gap

EFFECT OF EXCITATION FORCE DIRECTION

Although the results presented in Fig. 3 of the main are for an harmonic excitation with 45° inclination (i.e. $\mathbf{F}(t) = [F_x(t),\, F_y(t)] = [1,\, 1]F_0e^{-i\omega t}$), it is important to note that the one-way edge modes are not affected by the direction of the applied force. To clarify this point in Figs. S6, S7 and S8 we report results for the gyroscopic lattice excited by an harmonic force at 45°, 0° (horizontal excitation) and 90° (vertical excitation). The results clearly show that the one-way edge modes are not affected by the direction of the applied force.

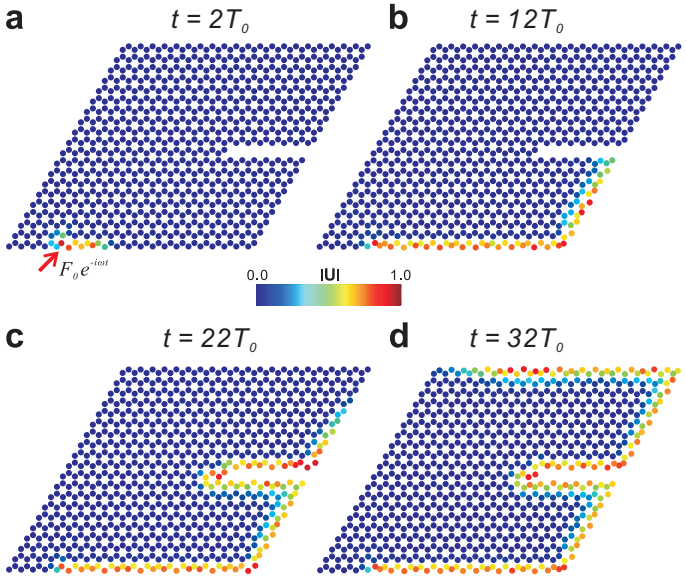

FIG. S6: **Transient Response** of a gyroscopic phononic crystal consisting of 20 × 20 unit cells with a line defect on the right boundary. Starting from $t = 0$, a time-harmonic excitation force $\mathbf{F}(t) = [F_x(t),\, F_y(t)] = [1,\, 1]F_0e^{-i\omega t}$ is prescribed at the site indicated by the red arrow. Snapshots of the displacement field at **(a)** $t = 2T_0$, **(b)** $t = 12T_0$, **(c)** $t = 22T_0$ and **(d)** $t = 32T_0$, where $T_0 = \sqrt{m_1/k_1}$ is the characteristic time scale of the system.

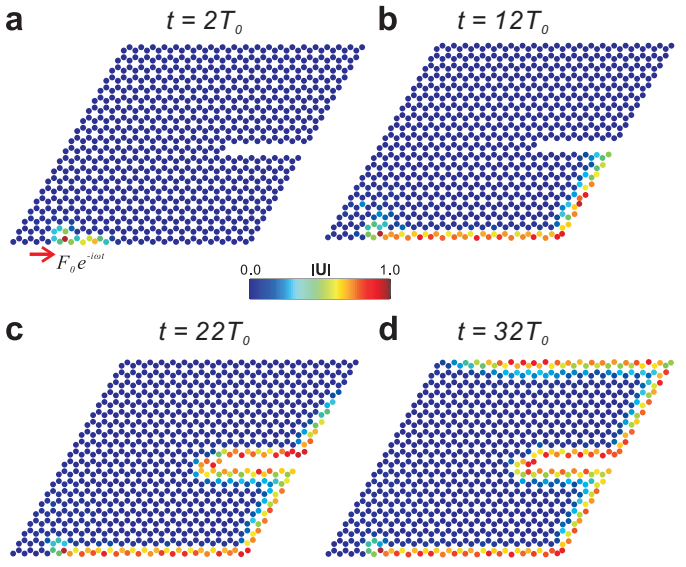

FIG. S7: **Transient Response** of a gyroscopic phononic crystal consisting of 20 × 20 unit cells with a line defect on the right boundary. Starting from $t = 0$, a time-harmonic excitation force $\mathbf{F}(t) = [F_x(t),\, F_y(t)] = [1,\, 0]F_0e^{-i\omega t}$ is prescribed at the site indicated by the red arrow. Snapshots of the displacement field at **(a)** $t = 2T_0$, **(b)** $t = 12T_0$, **(c)** $t = 22T_0$ and **(d)** $t = 32T_0$, where $T_0 = \sqrt{m_1/k_1}$ is the characteristic time scale of the system.

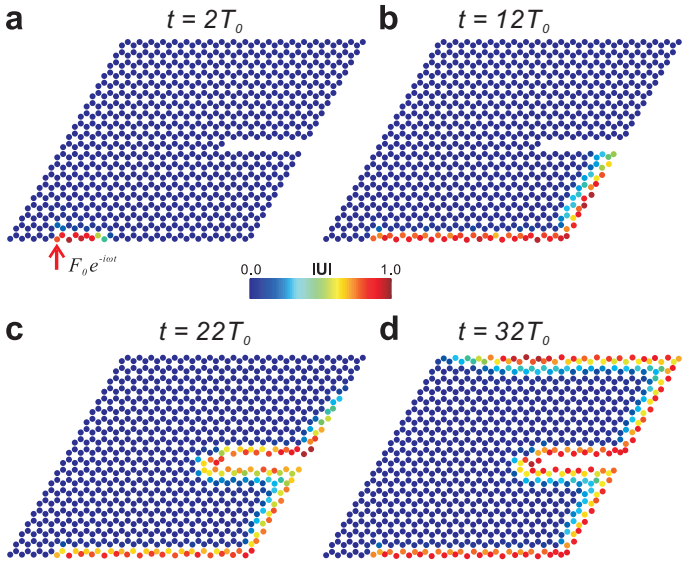

FIG. S8: **Transient Response** of a gyroscopic phononic crystal consisting of 20 × 20 unit cells with a line defect on the right boundary. Starting from $t = 0$, a time-harmonic excitation force $\mathbf{F}(t) = [F_x(t),\ F_y(t)] = [0,\ 1]F_0e^{-i\omega t}$ is prescribed at the site indicated by the red arrow. Snapshots of the displacement field at **(a)** $t = 2T_0$, **(b)** $t = 12T_0$, **(c)** $t = 22T_0$ and **(d)** $t = 32T_0$, where $T_0 = \sqrt{m_1/k_1}$ is the characteristic time scale of the system.

ADDITIONAL RESULTS FOR SQUARE LATTICE

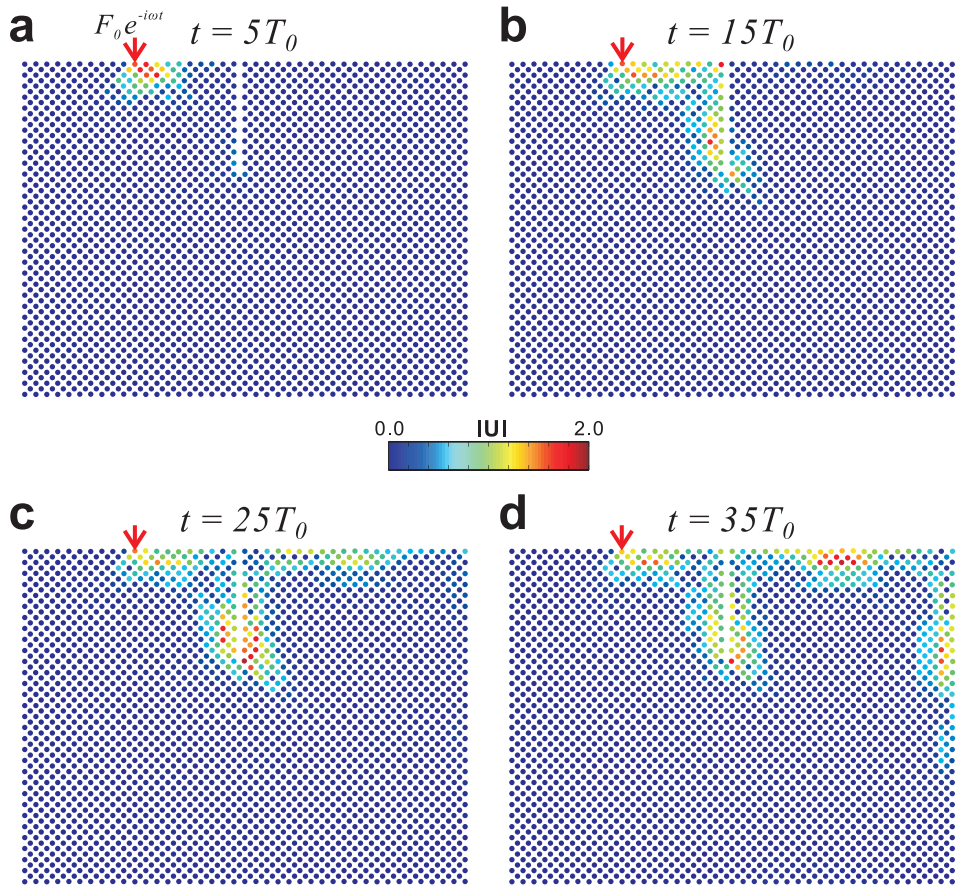

FIG. S9: **Transient Response** of a gyroscopic phononic crystal consisting of 40 × 30 square unit cells with a line defect on the top boundary: Snapshots of the velocity field at **(a)** $t = 5T_0$, **(b)** $t = 15T_0$, **(c)** $t = 25T_0$ and **(d)** $t = 35T_0$, where $T_0 = \sqrt{m_1/k_1}$ is the characteristic time scale of the system. Starting from $t = 0$, a time-harmonic excitation force $\mathbf{F}(t) = [F_x(t), F_y(t)] = [1, 1]F_0e^{-i\omega t}$ is prescribed at the site indicated by the red arrow.

FORMULATION OF GYROSCOPE

The gyroscope considered in this study has its top tip of the rotational axis pinned to a concentrated mass site in the phononic crystal, and the bottom tip pinned to the ground (Fig. S10). As a result, all translational motions at the base are prevented, while free rotations are allowed. Each gyroscope has 3 degrees of freedom described by the spin (ψ), precession (ϕ) and nutation (θ) angles with respect to the vertical z-axis, as shown in Fig. S10. Assuming constant spin and precession rates ($\dot{\psi} = \Psi$, $\dot{\phi} = \Phi$ and $\ddot{\psi} = \ddot{\phi} = 0$), its equations of motion can be written as [2–4]:

$$M_x = I_{xx}(\ddot{\theta} - \Phi^2 \sin\theta\cos\theta) + I_{zz}\Phi\sin\theta(\Phi\cos\theta + \Psi) \tag{S9}$$

$$M_y = (2I_{yy}\Phi\dot{\theta}\cos\theta) - I_{zz}\dot{\theta}(\Phi\cos\theta + \Psi))\sin\theta \tag{S10}$$

$$M_z = I_{zz}\Phi\dot{\theta}\sin\theta \tag{S11}$$

where M_x, M_y and M_z are moments about the x, y and z axes, respectively, and I_{xx}, I_{yy} and I_{zz} are the second moments of inertia. Note that in the absence of external moments $M_x = M_y = 0$ and that for symmetric gyroscopes (as those considered in this study) $I_{xx} = I_{yy} = I_0$.

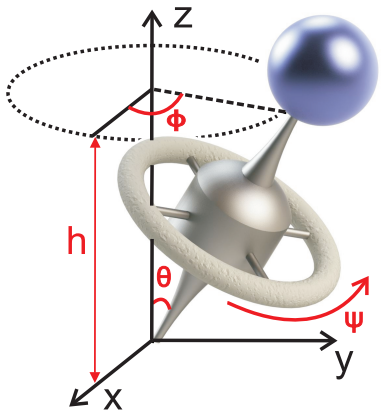

FIG. S10: **Gyroscope:** Schematic of a gyroscope with the top tip pinned to a mass in the lattice.

Here we consider a small amplitude time-harmonic in-plane motion at the top tip of the gyroscope induced by the lattice vibration,

$$U_{tip} = h\sin(\theta) \approx h\theta = h\Theta e^{i\omega t} \qquad \text{for} \quad |\Theta| \ll 1, \tag{S12}$$

where h is the height of the gyroscope. Under such assumption of small amplitude tip displacement ($\sin\theta \approx \theta$ and $\cos\theta \approx 1$), Eqn. (S10) can then be simplified to provide the relation between precession rate and spin rate,

$$\dot{\phi} = \Phi = \left(\frac{I_{zz}}{2I_0 - I_{zz}}\right)\Psi \tag{S13}$$

Moreover, substitution of Eqn. (S12) into Eqn. (S9) yields,

$$(I_{zz} - I_0)\Phi^2 + I_{zz}\Psi\Phi - I_0\omega^2 = 0 \tag{S14}$$

which can be combined with Eqn. (S13) to give

$$\Psi = \pm\omega\frac{2I_0 - I_{zz}}{I_{zz}} \tag{S15}$$

Note that, for $\omega = 0$, then $\Psi = 0$ implies that the gyroscope is not spinning and there is no rotational inertial coupling effect.

Finally, introducing Eqn. (S15) into Eqn. (S11), we arrive at

$$M_z = \pm\omega\dot{\theta}\theta I_{zz} = \pm i\omega^2\theta^2 I_{zz} \tag{S16}$$

Next, we determine the gyroscopic force F_g between the gyroscope and the concentrated mass pinned at its top. F_g is perpendicular to the direction of U_{tip} in the xy-plane and has to satisfy the balance of moment about the z-axis:

$$M_z = F_g h \sin\theta \approx F_g h\theta \tag{S17}$$

Combining Eqns. (S16) and (S17), we finally conclude that F_g takes the form

$$F_g = \pm i\frac{\omega^2}{h^2} I_{zz} U_{tip} \tag{S18}$$

Therefore, when the mass connected at the top tip of the gyroscope is displaced by $\mathbf{U}_{tip} = [u_x, u_y]$, the effective gyroscopic inertial force is given as:

$$\mathbf{F}_g = \pm i\frac{\omega^2}{h^2} I_{zz} \mathbf{R}\mathbf{U}_{tip}, \tag{S19}$$

where $\mathbf{R}$ is the rotation matrix,

$$\mathbf{R} = \begin{pmatrix} 0 & 1 \\ -1 & 0 \end{pmatrix} \tag{S20}$$

introduced to make the direction of $\mathbf{F}_g$ orthogonal to $\mathbf{U}_{tip}$.

Consequently, to take this rotational inertial effect into account, the mass matrix associated to each mass is given by

$$\tilde{\mathbf{M}} = \begin{pmatrix} m & i\alpha \\ -i\alpha & m \end{pmatrix}, \tag{S21}$$

where $\alpha = \pm I_{zz}/h^2$ represents the inertia coupling with a phase shift dictated by the imaginary multiplier i. This imaginary nature of the gyroscopic inertial effect indicates directional phase shifts between two independent directions of the tip displacements, which breaks time-reversal symmetry [5].

CALCULATION OF CHERN NUMBERS

We start by noting that the frequency-domain wave equation for a lattice is given by

$$\mathbf{K}(\boldsymbol{\mu})\mathbf{U} = \omega^2\tilde{\mathbf{M}}\mathbf{U}, \tag{S22}$$

where $\boldsymbol{\mu}$ is the Bloch-wave vector.

Solving Eqn. (S22) on the unit cell for wave vectors $\boldsymbol{\mu}$ within the first Brillouin zone, we obtain the dispersion relation $\omega = \omega(\boldsymbol{\mu})$ (eigenvalue) and the associated modal displacement vector field $\mathbf{U}(\boldsymbol{\mu})$ (eigenvector).

For a two-dimensional (2D) lattice, we use a $N_{\mu_1} \times N_{\mu_2}$ grid that covers the first Brillouin zone in the 2D $\boldsymbol{\mu}$-space. The modal displacement associated to the n-th band is then a vector field, $\mathbf{U}_n(\boldsymbol{\mu}) = \mathbf{U}_n(\mu_1, \mu_2)$ defined on a 2D discretized parametric domain.

In the following we focus on modal displacement associated to the n-th band (for the sake of simplicity, we drop the subscript n) and define the modal inner product as follows:

$$\langle \mathbf{U}(\boldsymbol{\mu})|\mathbf{U}(\boldsymbol{\mu}')\rangle = \mathbf{U}(\boldsymbol{\mu}) \cdot \tilde{\mathbf{M}}\mathbf{U}(\boldsymbol{\mu}') = \sum\nolimits_{p,q} U_p^*(\boldsymbol{\mu})\tilde{M}_{pq}U_q(\boldsymbol{\mu}') \tag{S23}$$

where U_p and U_q are components of vector $\mathbf{U}$, and $(\cdot)^*$ denotes the operation of complex conjugation.

Following an approach that is conceptually similar to the method proposed in [6], we calculate the Berry flux, $\tilde{F}_{12}$, for a small patch of the size $\Delta\mu_1 \times \Delta\mu_2$ on the $\boldsymbol{\mu}$-grid:

$$\tilde{F}_{12}(\boldsymbol{\mu}) = \ln\left(\frac{\langle \mathbf{U}(\boldsymbol{\mu})|\mathbf{U}(\boldsymbol{\mu}')\rangle \langle \mathbf{U}(\boldsymbol{\mu}')|\mathbf{U}(\boldsymbol{\mu}'')\rangle \langle \mathbf{U}(\boldsymbol{\mu}'')|\mathbf{U}(\boldsymbol{\mu}''')\rangle \langle \mathbf{U}(\boldsymbol{\mu}''')|\mathbf{U}(\boldsymbol{\mu})\rangle}{\langle \mathbf{U}(\boldsymbol{\mu})|\mathbf{U}(\boldsymbol{\mu})\rangle \langle \mathbf{U}(\boldsymbol{\mu}')|\mathbf{U}(\boldsymbol{\mu}')\rangle \langle \mathbf{U}(\boldsymbol{\mu}'')|\mathbf{U}(\boldsymbol{\mu}'')\rangle \langle \mathbf{U}(\boldsymbol{\mu}''')|\mathbf{U}(\boldsymbol{\mu}''')\rangle}\right), \tag{S24}$$

where $\boldsymbol{\mu} = (\mu_1, \mu_2)$, $\boldsymbol{\mu}' = (\mu_1 + \Delta\mu_1, \mu_2)$, $\boldsymbol{\mu}'' = (\mu_1 + \Delta\mu_1, \mu_2 + \Delta\mu_2)$ and $\boldsymbol{\mu}''' = (\mu_1, \mu_2 + \Delta\mu_2)$. Here $\tilde{F}_{12}$ is defined within the principal branch of the logarithm function, such that

$$-\pi < \frac{1}{i}\tilde{F}_{12}(\mu_1, \mu_2) \leq \pi \qquad \forall \mu_1, \mu_2 \quad . \tag{S25}$$

As shown in Ref. [6], we note that the denominator in Eqn. (S24) cannot vanish in order for it to be well defined. This condition can always be satisfied by a infinitesimal shift of the $N_{\mu_1} \times N_{\mu_2}$ grid in $\boldsymbol{\mu}$-space.

Finally, the numerical Chern number can be calculated by integrating the Berry flux over the entire first Brillouin zone:

$$C = \frac{1}{2\pi i}\sum_{\mu_1}\sum_{\mu_2}\tilde{F}_{12}(\mu_1, \mu_2). \tag{S26}$$

In addition, we note that when two or more bands share degenerate point(s) in band structure (e.g. the first and second bands always have a degeneracy at $\omega \to 0$), their combined Chern number should be calculated instead of individual ones.

To get the combined Chern number for the n-th and m-th bands, for instance, all four inner products of the form $\langle \mathbf{U}(\boldsymbol{\mu})|\mathbf{U}(\boldsymbol{\mu}')\rangle$ in the numerator of Eq. (S24) need to be replaced by the *determinant* of a 2×2 matrix $\mathbf{P}(\boldsymbol{\mu}, \boldsymbol{\mu}')$:

$$\mathbf{P}(\boldsymbol{\mu}, \boldsymbol{\mu}') = \begin{pmatrix} \langle \mathbf{U}_n(\boldsymbol{\mu})|\mathbf{U}_n(\boldsymbol{\mu}')\rangle & \langle \mathbf{U}_n(\boldsymbol{\mu})|\mathbf{U}_m(\boldsymbol{\mu}')\rangle \\ \langle \mathbf{U}_m(\boldsymbol{\mu})|\mathbf{U}_n(\boldsymbol{\mu}')\rangle & \langle \mathbf{U}_m(\boldsymbol{\mu})|\mathbf{U}_m(\boldsymbol{\mu}')\rangle \end{pmatrix}, \tag{S27}$$

If three or more bands are crossing each other, the matrix $\mathbf{P}(\boldsymbol{\mu}, \boldsymbol{\mu}')$ defined in Eq. (S27) can be easily generalized to a 3×3 or higher order matrix.

[1] M. Xiao, G. Ma, Z. Yang, P. Sheng, Z. Zhang, and C. Chan, Nature Physics **11**, 240 (2015).
[2] H. Goldstein, J. Safko, and C. Poole, *Classical Mechanics* (Addison-Wesley, 2002).
[3] M. Brun, I. S. Jones, and A. B. Movchan, Proceedings of the Royal Society of London A: Mathematical, Physical and Engineering Sciences **468**, 3027 (2012).
[4] G. Carta, M. Brun, A. Movchan, N. Movchan, and I. Jones, International Journal of Solids and Structures **51**, 2213 (2014).
[5] P. Wang and K. Bertoldi, *Towards phononic topological insulators*, Presented at APS March Meeting, A42.11 (2014).
[6] T. Fukui, Y. Hatsugai, and H. Suzuki, Journal of the Physical Society of Japan **74**, 1674 (2005).